Computers in Biology and Medicine 115 (2019) 103528

Contents lists available at ScienceDirect

Computers in Biology and Medicine

journal homepage: http://www.elsevier.com/locate/compbiomed

Synthesizing diffusion tensor imaging from functional MRI using fully convolutional networks

Seong-Jin Son [a,b,c], Bo-yong Park [d], Kyoungseob Byeon [a,b], Hyunjin Park [b,e,*]

[a] Department of Electronic and Computer Engineering, Sungkyunkwan University, South Korea
[b] Center for Neuroscience Imaging Research (CNIR), Institute for Basic Science, South Korea
[c] NEUROPHET Inc., South Korea
[d] McConnell Brain Imaging Centre, Montreal Neurological Institute and Hospital, McGill University, Montreal, Canada
[e] School of Electronic Electrical Engineering, Sungkyunkwan University, South Korea

ARTICLE INFO

Keywords:
Image synthesis
Deep learning
Fully convolutional network
Diffusion tensor imaging
Functional MRI

ABSTRACT

Purpose: Medical image synthesis can simulate a target modality of interest based on existing modalities and has the potential to save scanning time while contributing to efficient data collection. This study proposed a three-dimensional (3D) deep learning architecture based on a fully convolutional network (FCN) to synthesize diffusion-tensor imaging (DTI) from resting-state functional magnetic resonance imaging (fMRI).
Methods: fMRI signals derived from white matter (WM) exist and can be used for assessing WM alterations. We constructed an initial functional correlation tensor image using the correlation patterns of adjacent fMRI voxels as one input to the FCN. We considered T1-weighted images as an additional input to provide an algorithm with the structural information needed to synthesize DTI. Our architecture was trained and tested using a large-scale open database dataset (training n = 648; testing n = 293).
Results: The average correlation value between synthesized and actual diffusion tensors for 38 WM regions was 0.808, which significantly improves upon an existing study ($r = 0.480$). We also validated our approach using two open databases. Our proposed method showed a higher correlation with the actual diffusion tensor than the conventional machine-learning method for many WM regions.
Conclusions: Our method synthesized DTI images from fMRI images using a 3D FCN architecture. We hope to expand our method of synthesizing various other imaging modalities from a single image source.

1. Introduction

Neuroimaging plays an important role in diagnosing and establishing a treatment plan for various diseases [1]. Neuroimaging uses a variety of techniques to indirectly observe the structure and function of the brain [2]. Structural neuroimaging can detect abnormalities based on measures related to brain morphology or nerve-fiber bundles [3]. Diffusion tensor imaging (DTI) is a variant of magnetic resonance imaging (MRI) that is widely used to extract information about white matter (WM) fiber bundles [3]. Unlike structural neuroimaging, functional neuroimaging detects functional abnormalities in the brain, based on measures related to metabolism [4]. Functional MRI (fMRI) measures localized changes in cerebral blood flow related to neural activity using blood-oxygen-level-dependent (BOLD) contrast [4].

Recently, neuroimaging studies have moved toward adopting multi-modal approaches so that complementary information of the brain can be obtained in contrast to single-modal approaches [5]. One disadvantage of a multi-modal study is that the subjects must be scanned for each modality, which leads to increased time spent in the scanner [5]. Simply put, more resources are needed to perform multi-modal neuroimaging studies. One way to reduce the resource requirement is to perform medical image synthesis, which simulates a target modality of interest based on existing modalities. Image synthesis may be an option to reduce scan time and contribute to the efficient collection of data [6]. Many studies have adopted traditional machine learning approaches for medical image synthesis. Jog et al. synthesized T1- and T2-weighted contrast-enhanced MR images from T1-weighted, spoiled gradient recalled and double spin-echo images using the contrast learning on neighborhood ensembles [7]. Burgos et al. synthesized an attention map from the MR images instead of the computed tomography (CT) images

* Corresponding author.School of Electronic Electrical Engineering, Sungkyunkwan University, South Korea.
E-mail address: hyunjinp@skku.edu (H. Park).

https://doi.org/10.1016/j.compbiomed.2019.103528
Received 8 August 2019; Received in revised form 15 October 2019; Accepted 28 October 2019
Available online 31 October 2019

used for attenuation correction of positron emission tomography (PET) [8]. Bahrami et al. synthesized 7T MR images from 3T MR images using a hierarchical reconstruction-based canonical correlation analysis [9]. Many studies have also attempted medical image synthesis using deep learning models in various modalities [10–12]. Xiang et al. proposed a deep embedding convolutional neural network (CNN) for synthesizing CT images from T1-weighted MR images [12]. Xiang et al. also successfully estimated standard-dose PET images from low-dose PET-MRI images using deep auto-context CNN [10]. Nie et al. proposed an adversarial learning strategy based on FCN for synthesizing the CT from MR and 7T MR from 3T MR images [11]. Many of these studies attempted to synthesize one functional modality based on another functional modality or one structural modality based on another structural modality. It is likely more challenging to synthesize a structural modality (e.g., DTI) from a functional modality (e.g., fMRI), as the discrepancy between input and output modalities is large.

Various diffusion parameters (e.g., fractional anisotropy [FA] and mean diffusivity [MD]) can be calculated from DTI. The diffusion parameters can be used to detect WM anomalies in a variety of neurological and psychiatric disorders (e.g., Alzheimer's disease, Parkinson's disease, and schizophrenia) [3]. fMRI is generally used to observe brain activities in gray matter (GM) [4]. It is difficult to observe a BOLD signal in WM, as it contains about a quarter of the blood flow compared to GM [13,14]. Some studies have reported that fMRI activation can be observed in the genu and splenium of the corpus callosum [15,16]. BOLD signals were also observed in the internal capsule outside the corpus callosum [17]. The existence of vasculature, cerebral blood flow, and cerebral blood volume in the WM of fMRI may indicate the potential use of fMRIs to investigate WM.

In this study, we propose a 3D fully convolutional network (FCN) architecture to synthesize DTI images from resting-state fMRI images. We used a functional correlation tensor (FCT) from fMRI and T1-weighted images as input to the FCN model to synthesize DTI images. FCT is a dyadic tensor model based on the correlation of fMRI time series, and it shares a similar analytical framework with an actual DTI. We considered the T1-weighted image as an additional input to provide the algorithm with the structural information required to synthesize DTI images. The synthesized diffusion tensor obtained from the FCN was compared with the actual DTI image. The deep learning architecture was trained using the dataset of a large-scale open database (n = 648). We demonstrated the effectiveness of our approach by testing and validating various independent cohorts obtained from two open databases (n = 293, 45, and 102).

2. Methods

The method section is organized as follows. We begin by presenting the preprocessing of structural and functional imaging data in Section 2.1. Section 2.2 describes how to compute the initial FCT using the preprocessed fMRI data. Sections 2.3, 2.4, and 2.5 describe the proposed 3D FCN architecture (which is core to our image synthesis methodology), how the architecture includes various layers and loss function through implementation details, and the method used to evaluate the performance of the results. The overall pipeline is illustrated in Fig. 1.

2.1. Image preprocessing

MRI image data were preprocessed using software from AFNI and FSL [18,19]. T1-weighted structural MRI data were preprocessed using the following steps. Magnetic-field inhomogeneity was corrected, and non-brain tissues were removed by skull-stripping. The T1 data were spatially normalized to the Montreal Neurological Institute (MNI) space using a 9-parameter affine transformation. Rs-fMRI data were preprocessed using the following steps. The data taken during the first ten seconds were discarded to adjust for the hemodynamic response delay. Frame-wise displacement (FD) between time-series volumes was computed, and we removed the volumes with FD exceeding 0.5 mm. Head-motion correction and slice timing correction were also performed. Intensity normalization using a mean value of 10,000 was performed. Then, the fMRI data were registered onto the preprocessed T1-weighted data and then subsequently onto the MNI standard space using a 9-parameter affine transformation. We concatenated the two geometric transforms from the two registrations and applied the combined transform to the fMRI data. A band-pass filter passing frequency between 0.009 and 0.08 Hz was applied. Spatial smoothing of a full width at a half maximum (FWHM) of 4 mm was applied. The DTI data were reconstructed using the diffusion gradient table with the FDT toolbox in the FSL software [20,21]. DTI data were corrected for distortions caused by head-motion and eddy current artifacts. The corrected DTI data were registered onto the MNI standard space using the b0 image of the DTI data with a 9-parameter affine transformation. A diffusion tensor was estimated at each voxel of the brain using DTIFIT based on the least-squares model [20,21].

The preprocessed data were subtracted from its mean and divided by the variance to standardize image intensities across different modalities and to speed-up training [22]. Standardization was performed across voxels within a given subject. We cropped the images to include only the brain, minimizing the black background, thus obtaining a size of $80 \times 100 \times 100$ for each cropped image.

2.2. Initial FCT computation

Deep learning can work well if the input to the algorithm is similar to the intended output. The BOLD signal within each voxel of the fMRI image provides a time series with small amplitude fluctuations. We needed to compute directional information from fMRI data, and existing studies showed that correlation among neighborhood fMRI voxels could be used for that purpose [23–25]. The FCT for a given voxel can be computed from the covariance of adjacent voxels. We computed the initial FCT using the correlation values between the voxel, V_i, and its adjacent voxels in the fMRI image to use as input for our deep learning architecture. According to Ding et al., the FCT component, T_i, of a specific voxel, V_i, was calculated as follows [25].

$$T_i = \sum_{j=1}^{26} w_{ij} N_{ij}, \tag{1}$$

where w_{ij} was the soft thresholded and weighted Pearson's correlation coefficient between the time series V_i and V_j, as shown in Eq. (2) [25,

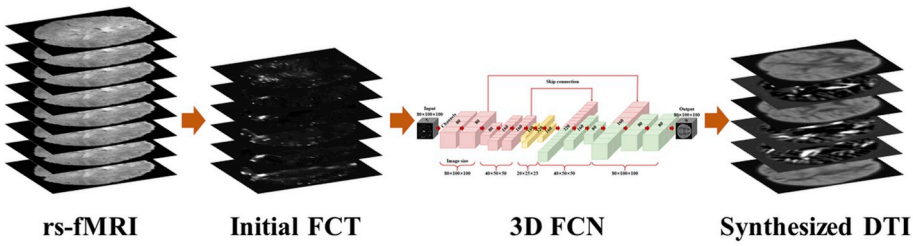

Fig. 1. The overall pipeline of our proposed method.

26].

$$w_{ij} = \left(\frac{r_{ij}+1}{2}\right)^{\beta}, \tag{2}$$

where r_{ij} was the correlation value of the time series between the voxel, V_i, and V_j; β was the scale-free index set to 12. N_{ij} was the dyadic tensor composed of unit vector $n_{ij} = [n_{ij,x}, n_{ij,y}, n_{ij,z}]^T$ between V_i and V_j [25,27,28].

$$N_{ij} = n_{ij}{n_{ij}}^T = \begin{bmatrix} n_{ij,x}n_{ij,x} & n_{ij,x}n_{ij,y} & n_{ij,x}n_{ij,z} \\ n_{ij,x}n_{ij,y} & n_{ij,y}n_{ij,y} & n_{ij,y}n_{ij,z} \\ n_{ij,x}n_{ij,z} & n_{ij,y}n_{ij,z} & n_{ij,z}n_{ij,z} \end{bmatrix}. \tag{3}$$

For a specific voxel, V_i, a total of 26 voxels, which were adjacent points in 3D space, are defined as V_j.

2.3. Fully convolutional networks for image synthesis

We used an end-to-end 3D deep learning architecture based on an FCN, which is widely used for image semantic segmentation [29–31]. The FCN maintains spatial information in the local neighborhood using a convolution layer instead of a fully connected layer in the standard convolutional neural network [32,33]. Whereas spatial information is maintained in the FCN, the input image inevitably loses its high-resolution information from the previous layer during the encoding process. This loss of spatial information makes it difficult to perform high-resolution up-sampling during the decoding process [32,33]. We added skip-connections to transfer data between both high- and low-level features in the encoder and decoder to help with effective and stable image representation.

In our architecture, input data consisted of seven channels. This includes six from the initial FCT and one from the preprocessed T1-weighted MR image, as the initial FCT is based on fMRI data only. Thus, the anatomical shape of the brain is not well represented. We included the anatomical information from the T1 data to help with the synthesis procedure. The output data consist of six channels corresponding to six elements of the diffusion tensor of DTI.

Many previous studies adopted a two-dimensional (2D) FCN [34,35]. In this study, we adopted 3D FCN, as the diffusion tensor has six elements (i.e., D_{xx}, D_{yy}, D_{zz}, D_{xy}, D_{yz}, and D_{xz}). Some of the elements are out-of-plane directions. The 3D structure is necessary to properly model those directions. The initial FCT used as the input of our proposed FCN is also calculated using a 3D kernel.

We show our proposed architecture in Fig. 2. The encoder has six layers containing convolution, average-pooling, batch normalization (BN), and rectified linear unit (ReLU) operations [32,36–39]. The encoder compresses meaningful information about high-dimensional input data and transfers it to a latent space, which compresses the most meaningful information of the input image [32,33]. The decoder has seven layers, containing up-sampling based on the nearest-neighbor interpolation, convolution, BN, and ReLU operations. We added skip connections between the encoder and decoder to help recover the full spatial information at the output. The kernel size of all convolutional layers, except latent space and the last layer, is $3 \times 3 \times 3$. The last layer only includes six convolution filters that match the diffusion tensor used as ground-truth. The numbers of filters are 80, 80, 80, 160, 160, 160, 320, 160, 320, 160, 80, 160, 80, 80, and 6, respectively, for individual layers.

2.4. Implementation details

The loss function used in training is shown Eq. (4).

$$L_{total}(Y_i, \widehat{Y}_i) = \frac{1}{n}\left(\sum_{i-1}^{n}(Y_i - \widehat{Y}_i)^2 + L_{gdl} + \lambda\sum_{i-1}^{n} w_i^2\right), \tag{4}$$

where Y_i is the actual diffusion tensor of DTI used as ground truth, $\widehat{Y}_i$ is the synthesized diffusion tensor by the output, n is the number of mini-batch input, and w_i is the sum of the weights. We used the L2 loss function as part of the fundamental loss function to measure the difference between the actual and synthesized DTI [40,41]. The second loss term is the gradient difference loss (GDL), which we adopt to avoid potential blurring from the L2 loss function [11]. The GDL is defined as

$$L_{gdl}(Y_i, \widehat{Y}_i) = \sum_{i=1}^{n}\Big(\big||\nabla Y_{i,x}| - |\nabla \widehat{Y}_{i,x}|\big|^2 + \big||\nabla Y_{i,y}| - |\nabla \widehat{Y}_{i,y}|\big|^2 + \big||\nabla Y_{i,z}| - |\nabla \widehat{Y}_{i,z}|\big|^2\Big). \tag{5}$$

The GDL helps minimize the difference of the magnitudes of the gradients between the actual and synthesized DTIs. The third loss term is the L2 regularization, which reduces the influence of outliers by preventing local noise and preventing the occurrence of overfitting, where the amount of training data is insufficient [42]. Using these loss terms, we seek to avoid blur and enhance details in the synthesized DTI.

The code was implemented using TensorFlow [43]. The above experiments were carried out on an NVIDIA Geforce GTX 1080 GPU. The networks were trained using the Adam optimizer with a learning rate of 10^{-4}, $\beta_1 = 0.5$, mini-batch size of 4, and a λ of L2 regularization of 0.5.

2.5. Evaluation

We applied our algorithm to the test set and the additional validation set to evaluate the performance of our proposed FCN architecture. Region-wise mean values of the synthesized DTI images were computed for the 38 WM regions, based on the ICBM DTI-81 atlas for each tensor [44]. We computed six correlation values between actual and

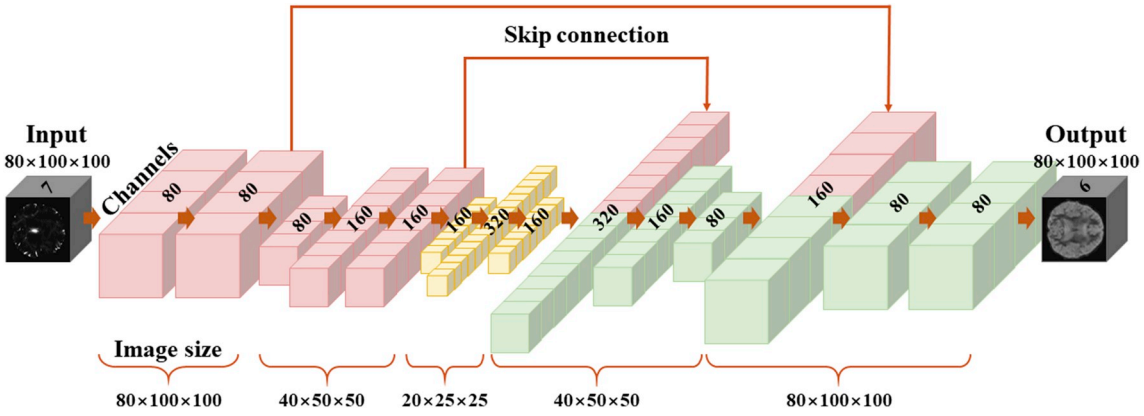

Fig. 2. The proposed 3D fully convolutional network for synthesizing the diffusion tensor from fMRI images.

synthesized DTI for all six channels (i.e., directions) in each voxel. The average correlation was computed for each voxel. Second, we took the regional mean from the average correlation from the voxels. We applied paired t-tests for 38 WM regions and compared various aspects of our FCN architecture; significance was assessed at $p < 0.05$ (false discovery rate corrected) [45].

2.6. Diseased state classification

Our architecture could be applied to data of any population. To see if our model could be applied to data of not only a healthy population but also a diseased population. We performed classification of the diseased state using the synthesized DTI images and compared results with classification results using the actual DTI images. Due to limited samples, we applied a leave-one-out cross-validation (LOOCV). FA and MD were calculated from the synthesized and actual diffusion DTI images, respectively. Discriminating features were selected using the least absolute shrinkage and selection operator (LASSO) for FA and MD. The classification was performed using a random forest (RF) using the selected features. The accuracy was calculated by comparing the predicted label with the actual label.

3. Results

3.1. Datasets

The Institutional Review Board (IRB) of Sungkyunkwan University approved this study. Our study was performed in full accordance with local IRB guidelines. Informed consent was obtained from all participants. Nine-hundred and forty-one subjects with T1-weighted MRI, rs-fMRI, and DTI data were obtained from the Human Connectome Project (HCP) database for training and testing of our method [46]. All subjects were scanned using a Siemens 3T scanner. T1-weighted MRI data were acquired using the magnetization prepared rapid gradient echo (MPRAGE) sequence (repetition time [TR] = 2400 ms, echo time [TE] = 2.14 ms, 0.7-mm isotropic voxels, and 260 slices). rs-fMRI data were acquired using the gradient-echo (GE) echo-planar imaging (EPI) sequence (TR = 720 ms, TE = 33.1 ms, 2.0 mm isotropic voxels, and 72 slices). DTI data were acquired using the spin-echo (SE) EPI sequence (TR = 5520 ms, TE = 89.5 ms, 1.25 mm isotropic voxels, 111 slices, and b-values = 3000 s/mm^2).

To validate our proposed method, two additional datasets were used. First, 45 subjects from the HCP retest dataset were obtained from the HCP database [46]. The 45 subjects from the initial HCP scanning stage were recruited to scan for a second time within 6 months of the first scan. The imaging protocols of all subjects were the same as the main HCP datasets described above. Second, data from 102 subjects from the Alzheimer's Disease Neuroimaging Initiative (ADNI) database were obtained [47]. The data consisted of normal controls (NC) (n = 52) and mild cognitive impairment (MCI) patients (n = 50). MCI is an intermediate stage between cognitively normal status and Alzheimer's disease (AD) [48]. MCI involves problems with memory, language, thinking, and judgment compared to normal people of their age, but the changes are not severe enough to interfere with daily life or independent function [49]. All subjects were scanned using a Siemens 3T scanner. T1-weighted MRI data were acquired using the MPRAGE sequence (TR = 2300 ms, TE = 2.95 ms, $1.2 \times 1.055 \times 1.055$ mm^3 voxel resolution, and 265 slices). rs-fMRI data were acquired using the GE EPI sequence (TR = 3000 ms, TE = 30 ms, 3.4 mm isotropic voxels, and 48 slices). DTI data were acquired using the SE EPI sequence (TR = 7200 ms, TE = 56 ms, 2.0 mm isotropic voxels, 80 slices, and b-values = 1000 s/mm^2).

3.2. Results of the training and testing stages

We randomly split the HCP dataset into training and testing sets. The split ratio was 70:30. Six-hundred and forty-eight subjects were used for training, and 293 subjects were used for testing. The training and testing loss plots per training epoch are given in Fig. 3. The testing was performed on the 39th epoch, which showed the best performance. It took approximately 15 min per epoch to train the model. Thus, the time required for learning was approximately 10 h.

The results of the testing were evaluated using Pearson's correlation in the 38 WM regions based on the ICBM DTI-81 atlas. We reported the name of regions and their corresponding correlation values between actual and synthesized diffusion tensor in Table 1. The genu of the corpus callosum showed the highest correlation value ($r = 0.889$). High correlation values were found in the corpus callosum and internal capsule. However, the left cingulum showed a low overall correlation value. The average correlation value for 38 WM regions was 0.808 (SD = 0.054) for the testing portion of the HCP dataset. This value is about twice as high as that obtained by using conventional machine learning in a previous study [23]. Fig. 4 presents the initial FCT, synthesized, and actual diffusion tensors according to the six elements of the diffusion tensor (*xx, yy, zz, xy, yz,* and *xz*), respectively.

3.3. Results of the validation stages

We used two datasets to validate our proposed method. First, 45 subjects obtained from the HCP retest dataset were validated. We reported region names and their corresponding correlation values for each validation set between actual and synthesized diffusion tensor in Table 2. The overall average correlation value for 38 WM ROIs was 0.793 (SD = 0.073) for the HCP retest dataset, which reflected the retest accuracy. The second validation dataset was different from the main dataset in terms of the included population (i.e., MCI cases added) and image acquisition settings. In carrying out the validation for this case, we applied the transfer learning approach [50]. The transfer learning allowed the initial weights of the previous model to be transferred to new unseen data for better initialization and convergence [50]. Our previously trained model using the HCP data of normal controls was transferred and subsequently adapted for new unseen data from ADNI that included both NC and MCI cases. We did not freeze any parts of the model. Thus, the model was updated using training data of NC (n = 30) and MCI (n = 30). The remaining data of NC (n = 20) and MCI (n = 22) were used as test data. Average Pearson's correlation between actual and synthesized DTI images for the NC of ADNI was 0.699 (SD = 0.097) and that for the MCI was 0.643 (SD = 0.088) computed over the 38 WM regions. The testing was performed on the 50th epoch.

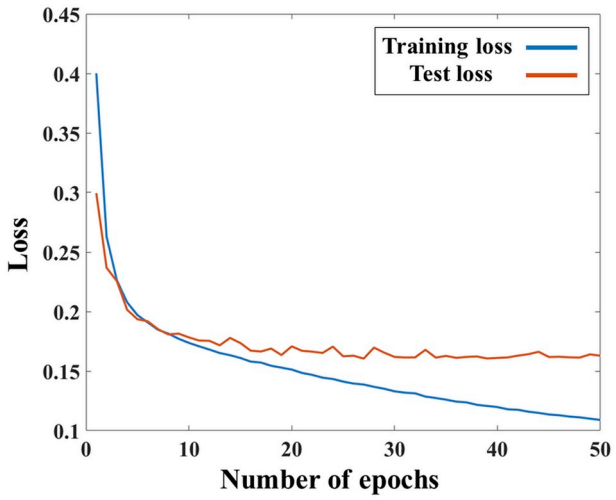

Fig. 3. Training and test loss plots with respect to the number of iterations.

Table 1
Pearson's correlation values for 38 WM regions between the synthesized and actual diffusion tensors in the test stage. Values were reported as the mean [standard deviation (SD)] and compared with a previous study using RF [23].

No.	ROI	Correlation value	
		Ding et al. method	Our proposed method
1	Genu of corpus callosum	0.418 (0.250)	0.889 (0.040)
2	Body of corpus callosum	0.338 (0.233)	0.864 (0.044)
3	Splenium of corpus callosum	0.538 (0.187)	0.868 (0.052)
4	Fornix	0.479 (0.301)	0.731 (0.167)
5	R. cerebral peduncle	0.737 (0.147)	0.820 (0.059)
6	L. cerebral peduncle	0.744 (0.142)	0.809 (0.044)
7	R. ant. limb of int. capsule	0.758 (0.157)	0.859 (0.043)
8	L. ant. limb of int. capsule	0.712 (0.177)	0.860 (0.052)
9	R. post. limb of int. capsule	0.791 (0.162)	0.881 (0.051)
10	L. post. limb of int. capsule	0.804 (0.117)	0.879 (0.062)
11	R. retro. part of int. capsule	0.593 (0.240)	0.844 (0.051)
12	L. retro. part of int. capsule	0.535 (0.227)	0.821 (0.046)
13	R. ant. corona radiate	0.513 (0.177)	0.862 (0.018)
14	L. ant. corona radiate	0.473 (0.190)	0.855 (0.021)
15	R. sup. corona radiate	0.575 (0.200)	0.830 (0.066)
16	L. sup. corona radiate	0.576 (0.171)	0.840 (0.060)
17	R. post. corona radiate	0.318 (0.240)	0.816 (0.047)
18	L. post. corona radiate	0.324 (0.220)	0.819 (0.038)
19	R. post. thalamic radiation	0.363 (0.215)	0.776 (0.046)
20	L. post. thalamic radiation	0.330 (0.233)	0.765 (0.050)
21	R. sagittal stratum	0.283 (0.229)	0.737 (0.068)
22	L. sagittal stratum	0.367 (0.189)	0.728 (0.057)
23	R. external capsule	0.647 (0.155)	0.876 (0.031)
24	L. external capsule	0.608 (0.171)	0.844 (0.028)
25	R. cingulum (cingulate gyrus)	0.226 (0.187)	0.779 (0.035)
26	L. cingulum (cingulate gyrus)	0.264 (0.222)	0.767 (0.045)
27	R. cingulum (hippocampus)	0.485 (0.239)	0.665 (0.074)
28	L. cingulum (hippocampus)	0.502 (0.217)	0.615 (0.074)
29	R. fornix/stria terminalis	0.348 (0.238)	0.815 (0.063)
30	L. fornix/stria terminalis	0.306 (0.220)	0.815 (0.046)
31	R. sup. longitudinal fasciculus	0.413 (0.238)	0.811 (0.047)
32	L. sup. longitudinal fasciculus	0.408 (0.218)	0.818 (0.045)
33	R. sup. fronto-occipital fasciculus	0.406 (0.282)	0.734 (0.099)
34	L. sup. fronto-occipital fasciculus	0.346 (0.388)	0.777 (0.082)
35	R. inf. fronto-occipital fasciculus	0.589 (0.274)	0.809 (0.055)
36	L. inf. fronto-occipital fasciculus	0.536 (0.323)	0.803 (0.070)
37	R. uncinated fasciculus	0.325 (0.271)	0.811 (0.045)
38	L. uncinated fasciculus	0.258 (0.288)	0.821 (0.037)
Overall		**0.480** (0.219)	**0.808 (0.054)**

3.4. Results of diseased state classification

We tested to see if the synthesized DTI images could be classified as either NC or diseased state (e.g., MCI), similar to actual DTI images. FA and MD values were computed from the synthesized DTI images and used to distinguish between NC and MCI using a classifier. In FA, we identified the anterior limb of the internal capsule, anterior corona radiata, hippocampus, and inferior fronto-occipital fasciculus as discriminating features. In MD, we identified the cerebral peduncle, external capsule, and uncinate fasciculus. Using all the features of FA and MD, the RF classifier achieved an accuracy of 73.81% to distinguish between NC and MCI.

We repeated the entire procedure using the actual DTI data. In FA, no features were selected via LASSO. In MD, we identified the sagittal stratum, external capsule, and uncinate fasciculus. Of note, the external capsule and uncinate fasciculus were the regions also found when synthesized DTI was used. Using all the features of FA and MD, the RF classifier achieved an accuracy of 78.57% to distinguish between NC and MCI. Using the actual DTI image led to better classification performance than using the synthesized DTI image. Still, synthesized DTI images were effective (better than the chance level of 52.38%) at distinguishing between NC and MCI.

3.5. Impact of T1-weighted MRI images

To show the contribution of including T1-weighted MR images to the input, we compared the use of only initial FCT images against the T1-weighted MR images. We showed the correlation values for each WM region in Table 3. If we used only the initial FCT images as input, the average correlation value would be 0.721, which would be 0.087 less than that resulting when the T1-weighted MR images were added. All 38 WM regions showed significant improvements between using only initial FCT images and on including the T1-weighted MR images. Thus, we demonstrated the effectiveness of including T1-weighted MR images in the input.

3.6. Impact of GDL

To show the contribution of the GDL function, we compared the inclusion and exclusion of the GDL function. We reported the correlation values for each WM region in Table 3. If we included the GDL function, the average correlation value for 38 WM regions would be 0.808. If we excluded the GDL function, the value would be 0.809. In terms of the average correlation value, there was no significant improvement. However, six regions among the 38 WM regions showed significant improvements. Therefore, the inclusion of the GDL function was effective for a few WM regions, but not for the entire WM.

3.7. Impact of skip connection

To demonstrate the effectiveness of using the skip connection, we compared the inclusion and the exclusion of the skip connection in our proposed architecture. There was no significant difference between them. However, significant improvement was observed in 24 of the 38 WM regions (Table 3). Therefore, the inclusion of the skip connection was effective for a few WM regions, which was similar to the trend we observed on including the GDL function.

4. Discussion

We synthesized DTI images from rs-fMRI images using a 3D FCN architecture. We first computed the initial FCT to transform the rs-fMRI images into a form similar to that of the actual diffusion tensor. The correlation between adjacent fMRI voxels could be close to one for many homogenous regions in the brain. However, there are regions whose voxels contain divergent fMRI time series data in a neighborhood, such as the transition region between inside and outside of the corpus callosum. Changes in local tissue property may cause changes in the fMRI time-series data, and we use the correlation of those fMRI data to train our deep learning model. The initial FCT and the preprocessed T1-weighted MRI images were used as input, and the actual diffusion tensor of DTI was used as ground-truth for our FCN architecture. The FCN architecture was trained and tested using the data from a large-scale database and further validated with two independent validation datasets.

The average correlation value for 38 WM regions using the test set of the HCP database was 0.808. In a previous study, DTI was also synthesized using an RF, and the value was 0.480 [23]. Therefore, our result showed a much higher correlation between synthesized and actual diffusion tensor than previous results. As mentioned in the introduction section, the BOLD signal was observed in the corpus callosum, internal capsule, and other WM regions [15–17]. In our results, the average correlations of the corpus callosum and internal capsule were 0.874 and 0.857, respectively. Our results were significantly better than those of previous studies using RFs with 0.431 and 0.698 in the same regions [23]. As with many other deep learning applications, our FCN

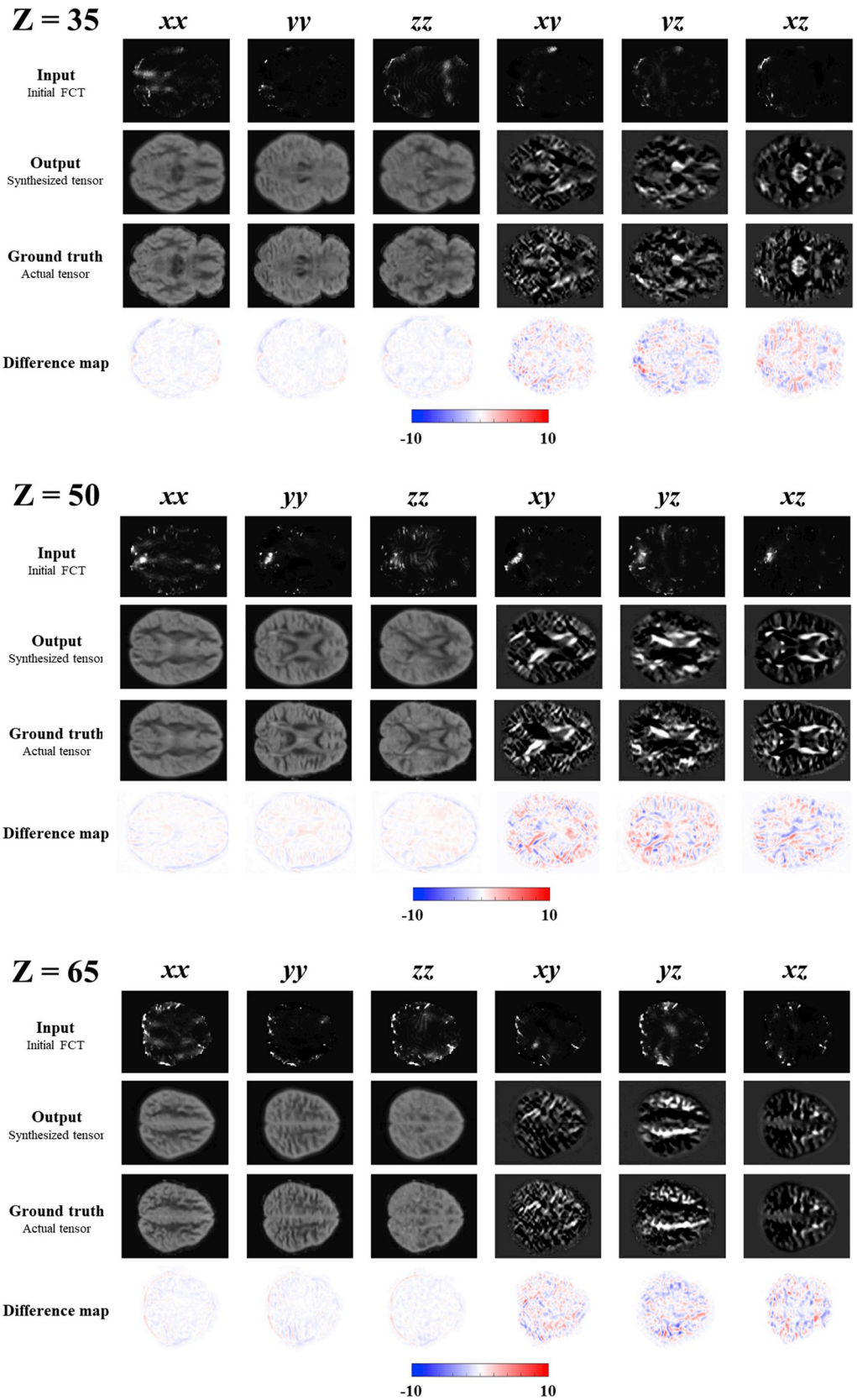

Fig. 4. Initial functional correlation tensor, synthesized diffusion tensor, and the actual diffusion tensor from one exemplary subject for three axial slices. The z-slice coordinate of the Montreal Neurological Institute space is given. Within each subfigure, the rows are the input, output, and ground truth of our proposed 3D fully convolutional network. The fourth row is a difference map showing the difference between the synthesized and the actual diffusion tensor.

Table 2
Pearson's correlation values for 38 WM regions between the synthesized and actual diffusion tensors in the validation stage. Values were reported as mean (SD).

No.	ROI	Correlation value		
		HCP retest dataset (n = 45)	ADNI dataset	
			NC (n = 22)	MCI (n = 20)
1	Genu of corpus callosum	0.861 (0.056)	0.701 (0.106)	0.652 (0.112)
2	Body of corpus callosum	0.823 (0.072)	0.778 (0.093)	0.733 (0.097)
3	Splenium of corpus callosum	0.832 (0.060)	0.849 (0.066)	0.826 (0.065)
4	Fornix	0.683 (0.236)	0.636 (0.180)	0.553 (0.183)
5	R. cerebral peduncle	0.794 (0.056)	0.707 (0.048)	0.664 (0.042)
6	L. cerebral peduncle	0.804 (0.058)	0.734 (0.033)	0.714 (0.017)
7	R. ant. limb of int. capsule	0.819 (0.050)	0.751 (0.072)	0.760 (0.051)
8	L. ant. limb of int. capsule	0.844 (0.055)	0.749 (0.079)	0.688 (0.043)
9	R. post. limb of int. capsule	0.863 (0.061)	0.721 (0.149)	0.734 (0.134)
10	L. post. limb of int. capsule	0.867 (0.067)	0.769 (0.118)	0.747 (0.106)
11	R. retro. part of int. capsule	0.810 (0.062)	0.740 (0.077)	0.671 (0.054)
12	L. retro. part of int. capsule	0.783 (0.071)	0.800 (0.032)	0.679 (0.070)
13	R. ant. corona radiate	0.824 (0.026)	0.694 (0.078)	0.636 (0.053)
14	L. ant. corona radiate	0.808 (0.032)	0.716 (0.056)	0.652 (0.045)
15	R. sup. corona radiate	0.784 (0.074)	0.745 (0.078)	0.697 (0.067)
16	L. sup. corona radiate	0.805 (0.073)	0.764 (0.080)	0.809 (0.078)
17	R. post. corona radiate	0.759 (0.052)	0.776 (0.035)	0.703 (0.049)
18	L. post. corona radiate	0.788 (0.040)	0.779 (0.056)	0.703 (0.046)
19	R. post. thalamic radiation	0.707 (0.078)	0.749 (0.059)	0.698 (0.079)
20	L. post. thalamic radiation	0.712 (0.081)	0.777 (0.024)	0.691 (0.038)
21	R. sagittal stratum	0.646 (0.103)	0.695 (0.067)	0.648 (0.076)
22	L. sagittal stratum	0.667 (0.081)	0.703 (0.072)	0.591 (0.074)
23	R. external capsule	0.839 (0.054)	0.646 (0.138)	0.624 (0.116)
24	L. external capsule	0.804 (0.051)	0.661 (0.156)	0.604 (0.125)
25	R. cingulum(cingulate gyrus)	0.721 (0.046)	0.598 (0.140)	0.559 (0.139)
26	L. cingulum(cingulate gyrus)	0.695 (0.046)	0.588 (0.154)	0.518 (0.145)
27	R. cingulum (hippocampus)	0.654 (0.079)	0.616 (0.048)	0.598 (0.051)
28	L. cingulum (hippocampus)	0.578 (0.074)	0.611 (0.054)	0.504 (0.027)
29	R. fornix/stria terminalis	0.757 (0.070)	0.710 (0.121)	0.698 (0.048)
30	L. fornix/stria terminalis	0.734 (0.096)	0.751 (0.050)	0.671 (0.045)
31	R. sup. longitudinal fasciculus	0.772 (0.037)	0.637 (0.115)	0.566 (0.111)
32	L. sup. longitudinal fasciculus	0.778 (0.043)	0.668 (0.130)	0.577 (0.099)
33	R. sup. fronto-occipital fasciculus	0.632 (0.153)	0.704 (0.105)	0.659 (0.118)
34	L. sup. fronto-occipital fasciculus	0.695 (0.117)	0.722 (0.091)	0.574 (0.144)
35	R. inf. fronto-occipital fasciculus	0.753 (0.093)	0.528 (0.199)	0.497 (0.172)
36	L. inf. fronto-occipital fasciculus	0.755 (0.112)	0.579 (0.231)	0.509 (0.194)
37	R. uncinated fasciculus	0.771 (0.066)	0.585 (0.107)	0.543 (0.095)
38	L. uncinated fasciculus	0.776 (0.052)	0.641 (0.194)	0.594 (0.122)
Overall		**0.763 (0.072)**	**0.699 (0.097)**	**0.643 (0.088)**

significantly improved the results obtained from conventional machine learning, which demonstrates the effectiveness of deep learning approaches in the field of medical image synthesis [34,35]. The impacts of input data types and components on our model are found in the supplemental materials.

The diffusion tensor of DTI consists of six elements (D_{xx}, D_{yy}, D_{zz}, D_{xy}, D_{yz}, and D_{xz}) [3]. The three diagonal elements (D_{xx}, D_{yy}, and D_{zz}) are proportional to the diffusion displacement variances along the principal (x-, y-, and z-) laboratory axes. The three off-diagonal elements (D_{xy}, D_{yz}, and D_{xz}) are proportional to the correlation of displacements between each pair of principal directions. Biological tissue demonstrates some degree of anisotropy [3]. In particular, WM is highly anisotropic because of its parallel orientation of nerve fiber tracts. Thus, there are significant variations in off-diagonal elements of DTI in WM, owing to the anisotropy. The high variability of the off-diagonal elements is readily shown as images of fast-varying texture patterns, compared to less-varying texture patterns of diagonal elements, as shown in Fig. 4. In the difference map (the last row of the sub figures in Fig. 4), the difference between the synthesized and the actual diffusion tensor of the off-diagonal elements appears to be larger than the difference of the diagonal elements. These differences may not come from the algorithmic deficit. Instead, they could be differences from the nature of the elements. The correlation values between synthesized and actual diffusion tensor for six elements (D_{xx}, D_{yy}, D_{zz}, D_{xy}, D_{yz}, and D_{xz}) in 38 WM regions were 0.778, 0.808, 0.812, 0.813, 0.827, and 0.812, respectively. The correlation values were similar across all six elements. This showed that our algorithm synthesized all six elements well, not only the diagonal elements.

We applied our approach to independent validation datasets. The first validation dataset was from the HCP retest dataset. In the HCP retest dataset, a subset of subjects from the original HCP dataset was recruited again for the retest experiments, and thus, those subjects were included both in the original and the retest of the HCP dataset. As the same subjects appeared in both data, the HCP retest dataset was not totally independent data from the original HCP dataset. Thus, the accuracy reported with the HCP retest dataset should be interpreted as retest accuracy. The HCP retest dataset shared the same image acquisition settings, and thus, there was no need to adjust the trained model. We applied the trained model without transfer learning to the HCP retest dataset. On the other hand, the ADNI dataset had different image acquisition settings; consequently, the ADNI had a potentially different image quality. Therefore, we applied the transfer learning to validation dataset. Validation using the HCP retest dataset ($r = 0.793$) did not show a significant decrease in the average correlation compared to that of the HCP test dataset ($r = 0.808$). However, the correlation value decreased when the ADNI dataset (NC: $r = 0.699$ and MCI: $r = 0.643$) was validated. This degradation may be caused by the difference in image quality across different databases [51,52]. Although transfer learning was adopted to adjust our model for the ADNI dataset, the performance of the ADNI dataset was lower than that of the HCP dataset.

Table 3
Pearson's correlation values for 38 WM regions between the synthesized and actual diffusion tensors for various comparisons. Values were reported as mean (SD). Significant improvement ($p < 0.05$, false discovery rate corrected) in the correlation between our proposed method, and each comparison case is shown in bold and marked with an asterisk.

No.	ROI	Correlation value			
		Proposed method	No T1	No GDL	No skip connection
1	Genu of corpus callosum	0.889 (0.040)	***0.838 (0.069)**	0.889 (0.039)	***0.887 (0.041)**
2	Body of corpus callosum	0.864 (0.044)	***0.806 (0.065)**	0.868 (0.043)	0.863 (0.044)
3	Splenium of corpus callosum	0.868 (0.052)	***0.800 (0.088)**	***0.864 (0.053)**	0.869 (0.052)
4	Fornix	0.731 (0.167)	***0.666 (0.168)**	0.735 (0.163)	0.726 (0.183)
5	R. cerebral peduncle	0.820 (0.059)	***0.777 (0.069)**	0.819 (0.056)	***0.812 (0.058)**
6	L. cerebral peduncle	0.809 (0.044)	***0.755 (0.065)**	***0.803 (0.050)**	***0.791 (0.052)**
7	R. ant. limb of int. capsule	0.859 (0.043)	***0.788 (0.085)**	0.862 (0.036)	***0.856 (0.044)**
8	L. ant. limb of int. capsule	0.860 (0.052)	***0.799 (0.087)**	0.860 (0.047)	***0.855 (0.044)**
9	R. post. limb of int. capsule	0.881 (0.051)	***0.835 (0.071)**	0.882 (0.052)	***0.878 (0.055)**
10	L. post. limb of int. capsule	0.879 (0.062)	***0.825 (0.103)**	***0.874 (0.069)**	***0.871 (0.068)**
11	R. retro. part of int. capsule	0.844 (0.051)	***0.769 (0.075)**	***0.839 (0.050)**	0.842 (0.054)
12	L. retro. part of int. capsule	0.821 (0.046)	***0.730 (0.093)**	0.826 (0.046)	0.822 (0.052)
13	R. ant. corona radiate	0.862 (0.018)	***0.792 (0.037)**	0.863 (0.017)	0.861 (0.019)
14	L. ant. corona radiate	0.855 (0.021)	***0.785 (0.042)**	0.855 (0.020)	0.855 (0.020)
15	R. sup. corona radiate	0.830 (0.066)	***0.738 (0.095)**	0.832 (0.063)	0.830 (0.064)
16	L. sup. corona radiate	0.840 (0.060)	***0.744 (0.095)**	0.842 (0.057)	***0.836 (0.061)**
17	R. post. corona radiate	0.816 (0.047)	***0.738 (0.058)**	0.819 (0.042)	0.820 (0.043)
18	L. post. corona radiate	0.819 (0.038)	***0.717 (0.046)**	0.817 (0.041)	***0.816 (0.039)**
19	R. post. thalamic radiation	0.776 (0.046)	***0.675 (0.092)**	0.775 (0.045)	***0.769 (0.049)**
20	L. post. thalamic radiation	0.765 (0.050)	***0.639 (0.099)**	0.767 (0.047)	0.764 (0.052)
21	R. sagittal stratum	0.737 (0.068)	***0.618 (0.117)**	0.735 (0.067)	***0.728 (0.071)**
22	L. sagittal stratum	0.728 (0.057)	***0.573 (0.123)**	0.733 (0.056)	***0.719 (0.059)**
23	R. external capsule	0.876 (0.031)	***0.806 (0.056)**	***0.872 (0.031)**	***0.872 (0.031)**
24	L. external capsule	0.844 (0.028)	***0.760 (0.063)**	0.844 (0.023)	0.846 (0.029)
25	R. cingulum (cingulate gyrus)	0.779 (0.035)	***0.639 (0.056)**	0.779 (0.041)	***0.774 (0.033)**
26	L. cingulum (cingulate gyrus)	0.767 (0.045)	***0.592 (0.085)**	0.767 (0.050)	***0.761 (0.047)**
27	R. cingulum (hippocampus)	0.665 (0.074)	***0.553 (0.097)**	0.665 (0.075)	***0.655 (0.078)**
28	L. cingulum (hippocampus)	0.615 (0.074)	***0.480 (0.106)**	0.623 (0.063)	***0.599 (0.075)**
29	R. fornix/stria terminalis	0.815 (0.063)	***0.752 (0.108)**	0.819 (0.057)	***0.811 (0.060)**
30	L. fornix/stria terminalis	0.815 (0.046)	***0.754 (0.060)**	0.817 (0.046)	***0.800 (0.041)**
31	R. sup. longitudinal fasciculus	0.811 (0.047)	***0.711 (0.075)**	0.811 (0.046)	***0.804 (0.049)**
32	L. sup. longitudinal fasciculus	0.818 (0.045)	***0.703 (0.079)**	0.818 (0.045)	0.816 (0.044)
33	R. sup. fronto-occipital fasciculus	0.734 (0.099)	***0.624 (0.114)**	0.739 (0.094)	0.736 (0.093)
34	L. sup. fronto-occipital fasciculus	0.777 (0.082)	***0.686 (0.099)**	0.774 (0.073)	***0.760 (0.074)**
35	R. inf. fronto-occipital fasciculus	0.809 (0.055)	***0.711 (0.121)**	0.810 (0.052)	***0.796 (0.068)**
36	L. inf. fronto-occipital fasciculus	0.803 (0.070)	***0.721 (0.133)**	0.805 (0.064)	***0.792 (0.086)**
37	R. uncinated fasciculus	0.811 (0.045)	***0.744 (0.062)**	0.820 (0.049)	0.811 (0.047)
38	L. uncinated fasciculus	0.821 (0.037)	***0.752 (0.079)**	***0.813 (0.040)**	***0.789 (0.049)**
Overall		**0.808 (0.054)**	**0.721 (0.085)**	**0.809 (0.053)**	**0.802 (0.056)**

Nevertheless, our approach showed a higher performance than previous studies using conventional machine learning [23].

We performed classification using the synthesized DTI image derived from the ADNI dataset to see if our model can be used to distinguish between diseased and normal states compared to using actual DTI images for the classification. The RF classifier was used to distinguish between NC and MCI using the selected features via LASSO. In the synthesized diffusion tensor, four FA values and three MD values were selected, and in the actual diffusion tensor, three MD values were selected. We identified the hippocampus as the significant feature to distinguish between NC and MCI among the features used in the classification of the synthesized diffusion tensor. The hippocampus is known to be affected by the progression of MCI and AD [53,54]. In addition, the external capsule and uncinate fasciculus regions were commonly selected in the classification of synthesized and actual diffusion tensor images. These regions were also reported to be affected by the progression of MCI and AD in studies using DTI [55–58]. The RF classifier using synthesized DTI images achieved an accuracy of 73.81% in distinguishing between NC and MCI. Using the actual DTI images, the classifier achieved an accuracy of 78.57%. Synthesized DTI was effective (better than the chance level of 52.38%) at distinguishing between NC and MCI. As a result, we confirmed that the synthesized DTI contained enough information to distinguish between normal and diseased states for AD compared to the actual DTI. We also report the average correlation of the FA and MD values over the 38 WM regions between synthesized and actual DTI for all datasets in the Supplement.

We employed a resize-convolution layer, using nearest-neighbor interpolation instead of a deconvolution layer at the up-sampling stage in our architecture [59,60]. Resize-convolution is a method of up-sampling with reduced resolution using nearest-neighbor interpolation and then applying a standard convolution. Many studies have used a deconvolution layer to perform up-sampling [61–64]. The simple deconvolution suffers from checkerboard artifacts. There are two reported reasons for this [59,60]. One is the deconvolution overlap caused by the unmatched kernel size of the deconvolution with respect to the stride. Another is the random initialization problem. When we adopted two consecutive deconvolutions, the artifacts were prevalent. Thus, we employed the resize-convolution proposed by Odena et al. [60].

Our study has some limitations. First, we used correlation, not an error metric (such as the L2 norm), between synthesized and actual diffusion tensor to assess the performance of our approach. This is because MRI does not have a unit. There could be scaling differences among multi-center datasets [51,52]. Thus, we adopted a correlation to remove the effects of scaling. There are efforts to better normalize MRI data between multi-center settings. Thus, future research should consider those. Second, the number of training data was insufficient. The HCP database is one of the largest neuroimaging databases. We used more than 600 subjects from the HCP database to train our architecture. The sample size might be large in the neuroimaging community, but it is quite small compared to other research fields, where one can find

thousands or tens of thousands of samples [34,35]. Larger neuroimaging databases are actively developed, and they will be made available soon [65]. Meanwhile, researchers should adopt deep learning approaches that require fewer samples, such as transfer learning and one-shot learning to neuroimaging. Third, the goal of medical image synthesis is to construct a target modality of interest (i.e., DTI) based on existing modalities (i.e., fMRI and T1-weighted data). If successful, medical image synthesis should be able to fully replicate the actual data. Our study showed that a high correlation between actual and synthesized DTI exists. Still, further validations using large-scale independent data are necessary to make medical synthesis approaches clinically feasible.

5. Conclusion

Our study showed the potential to construct DTI images from fMRI data. An initial functional correlation tensor was constructed from fMRI data and used as input along with the T1-weighted anatomical information to synthesize actual DTI images using our 3D FCN. Validation of our model was performed on healthy normal subjects and diseased subjects. Results of validations showed a higher correlation with the actual diffusion tensor than did previous studies based on conventional machine learning. In addition, the classification performance of the disease status using the synthesized diffusion tensor was similar to that using the actual diffusion tensor. We hope to apply our algorithm to find better biomarkers for diseases, such as Alzheimer's or Parkinson's disease.

Declaration of competing interest

None declared.

Acknowledgments

This work was supported by the Institute for Basic Science (IBS-R015-D1), the National Research Foundation of Korea (NRF-2019R1H1A2079721), the Ministry of Science and ICT of Korea under the Information Technology Research Center support program (IITP-2019-2018-0-01798), the IITP grant funded by the Korean government under the AI Graduate School Support Program (2019-0-00421), and Research and Business Development Program through the Korea Institute for Advancement of Technology (KIAT) funded by the Ministry of Trade, Industry and Energy (MOTIE) (P049700065).

Appendix A. Supplementary data

Supplementary data to this article can be found online at https://doi.org/10.1016/j.compbiomed.2019.103528.

References

[1] D.T. Willingham, E.W. Dunn, What neuroimaging and brain localization can do, cannot do and should not do for social psychology, J. Personal. Soc. Psychol. 85 (2003) 662–671, https://doi.org/10.1037/0022-3514.85.4.662.

[2] V.P.B. Grover, J.M. Tognarelli, M.M.E. Crossey, I.J. Cox, S.D. Taylor-Robinson, M. J.W. McPhail, Magnetic resonance imaging: principles and techniques: lessons for clinicians, J. Clin. Exp. Hepatol. 5 (2015) 246–255, https://doi.org/10.1016/j.jceh.2015.08.001.

[3] S. Mori, J. Zhang, Principles of diffusion tensor imaging and its applications to basic neuroscience research, Neuron 51 (2006) 527–539, https://doi.org/10.1016/j.neuron.2006.08.012.

[4] J.C. Gore, Principles and practice of functional MRI of the human brain, J. Clin. Investig. 112 (2003) 4–9, https://doi.org/10.1172/JCI200319010.

[5] S. Liu, W. Cai, S. Liu, F. Zhang, M. Fulham, D. Feng, S. Pujol, R. Kikinis, Multimodal neuroimaging computing: a review of the applications in neuropsychiatric disorders, Brain Inf. 2 (2015) 167–180, https://doi.org/10.1007/s40708-015-0019-x.

[6] A. Beers, J. Brown, K. Chang, J.P. Campbell, S. Ostmo, M.F. Chiang, J. Kalpathy-Cramer, High-resolution Medical Image Synthesis Using Progressively Grown Generative Adversarial Networks, 2018, pp. 1–8, arXiv:1805.03144.

[7] A. Jog, C. Aaron, S. Roy, D.L. Pham, J.L. Prince, MR image synthesis by contrast learning on neighborhood ensembles, Med. Image Anal. 24 (2015) 63–76, https://doi.org/10.1016/j.media.2015.05.002.

[8] N. Burgos, M.J. Cardoso, K. Thielemans, M. Modat, J. Dickson, J.M. Schott, D. Atkinson, S.R. Arridge, B.F. Hutton, Sébastien Ourselin, Multi-contrast attenuation map synthesis for PET/MR scanners: assessment on FDG and Florbetapir PET tracers, Eur. J. Nucl. Med. Mol. Imaging 42 (2015) 1447–1458, https://doi.org/10.1007/s00259-015-3082-x.

[9] K. Bahrami, F. Shi, X. Zong, H.W. Shin, H. An, D. Shen, Reconstruction of 7T-like images from 3T MRI, IEEE Trans. Med. Imaging 35 (2016) 2085–2097, https://doi.org/10.1109/TMI.2016.2549918.

[10] L. Xiang, Y. Qiao, D. Nie, L. An, Q. Wang, D. Shen, Deep auto-context convolutional neural networks for standard-dose PET image estimation from low-dose PET/MRI, Neurocomputing 267 (2017) 406–416, https://doi.org/10.1016/j.neucom.2017.06.048.

[11] D. Nie, R. Trullo, J. Lian, L. Wang, C. Petitjean, S. Ruan, Q. Wang, D. Shen, Medical image synthesis with deep convolutional adversarial networks, IEEE Trans. Biomed. Eng. 9294 (2018) 1–11, https://doi.org/10.1109/TBME.2018.2814538.

[12] L. Xiang, Q. Wang, D. Nie, L. Zhang, X. Jin, Y. Qiao, D. Shen, Deep embedding convolutional neural network for synthesizing CT image from T1-Weighted MR image, Med. Image Anal. 47 (2018) 31–44, https://doi.org/10.1016/j.media.2018.03.011.

[13] H. Nonaka, M. Akima, T. Hatori, T. Nagayama, Z. Zhang, F. Ihara, The microvasculature of the cerebral white matter: arteries of the deep white matter, J. Neuropathol. Exp. Neurol. 62 (2003) 154–161, https://doi.org/10.1093/jnen/62.2.154.

[14] M.E. Raichle, A.Z. Snyder, A default mode of brain function: a brief history of an evolving idea, Neuroimage 37 (2007) 1083–1090, https://doi.org/10.1016/j.neuroimage.2007.02.041.

[15] R.C.N. D'Arcy, A. Hamilton, M. Jarmasz, S. Sullivan, G. Stroink, Exploratory data analysis reveals visuovisual interhemispheric transfer in functional magnetic resonance imaging, Magn. Reson. Med. 55 (2006) 952–958, https://doi.org/10.1002/mrm.20839.

[16] M. Tettamanti, E. Paulesu, P. Scifo, A. Maravita, F. Fazio, D. Perani, C.A. Marzi, Interhemispheric transmission of visuomotor information in humans: fMRI evidence, J. Neurophysiol. 88 (2002) 1051–1058, https://doi.org/10.1152/jn.2002.88.2.1051.

[17] E.L. Mazerolle, R.C. D'Arcy, S.D. Beyea, Detecting functional magnetic resonance imaging activation in white matter: interhemispheric transfer across the corpus callosum, BMC Neurosci. 9 (2008) 84, https://doi.org/10.1186/1471-2202-9-84.

[18] M. Jenkinson, C.F. Beckmann, T.E.J. Behrens, M.W. Woolrich, S.M. Smith, FSL, Neuroimage 62 (2012) 782–790, https://doi.org/10.1016/j.neuroimage.2011.09.015.

[19] R.W. Cox, AFNI: software for analysis and visualization of functional magnetic resonance neuroimages, Comput. Biomed. Res. 29 (1996) 162–173, https://doi.org/10.1006/cbmr.1996.0014.

[20] T.E.J. Behrens, M.W. Woolrich, M. Jenkinson, H. Johansen-Berg, R.G. Nunes, S. Clare, P.M. Matthews, J.M. Brady, S.M. Smith, Characterization and propagation of uncertainty in diffusion-weighted MR imaging, Magn. Reson. Med. 50 (2003) 1077–1088, https://doi.org/10.1002/mrm.10609.

[21] T.E.J. Behrens, H.J. Berg, S. Jbabdi, M.F.S. Rushworth, M.W. Woolrich, Probabilistic diffusion tractography with multiple fibre orientations: what can we gain? Neuroimage 34 (2007) 144–155, https://doi.org/10.1016/j.neuroimage.2006.09.018.

[22] Y. LeCun, P. Haffner, L. Bottou, Y. Bengio, Object recognition with gradient-based learning, Proc. IEEE 86 (1999) 319–345, https://doi.org/10.1007/3-540-46805-6_19.

[23] L. Zhang, H. Zhang, X. Chen, Q. Wang, P.T. Yap, D. Shen, Learning-based structurally-guided construction of resting-state functional correlation tensors, Magn. Reson. Imaging 43 (2017) 110–121, https://doi.org/10.1016/j.mri.2017.07.008.

[24] Z. Ding, A.T. Newton, R. Xu, A.W. Anderson, V.L. Morgan, J.C. Gore, Spatio-temporal correlation tensors reveal functional structure in human brain, PLoS One 8 (2013), e82107, https://doi.org/10.1371/journal.pone.0082107.

[25] Z. Ding, R. Xu, S.K. Bailey, T.-L. Wu, V.L. Morgan, L.E. Cutting, A.W. Anderson, J. C. Gore, Visualizing functional pathways in the human brain using correlation tensors and magnetic resonance imaging, Magn. Reson. Imaging 34 (2016) 8–17, https://doi.org/10.1016/j.mri.2015.10.003.

[26] A.J. Schwarz, J. McGonigle, Negative edges and soft thresholding in complex network analysis of resting state functional connectivity data, Neuroimage 55 (2011) 1132–1146, https://doi.org/10.1016/j.neuroimage.2010.12.047.

[27] P.J. Basser, S. Pajevic, Statistical artifacts in diffusion tensor MRI (DT-MRI) caused by background noise, Magn. Reson. Med. 44 (2000) 41–50, https://doi.org/10.1002/1522-2594(200007)44:1<41::AID-MRM8>3.0.CO;2-O.

[28] Y. Zhou, H. Zhang, L. Zhang, X. Cao, R. Yang, Q. Feng, P.T. Yap, D. Shen, Functional MRI registration with tissue-specific patch-based functional correlation tensors, Hum. Brain Mapp. (2018) 1–14, https://doi.org/10.1002/hbm.24021.

[29] L. Bi, D. Feng, J. Kim, Dual-path adversarial learning for fully convolutional network (FCN)-Based medical image segmentation, Vis. Comput. 34 (2018) 1043–1052, https://doi.org/10.1007/s00371-018-1519-5.

[30] P.F. Christ, F. Ettlinger, F. Grün, M.E.A. Elshaera, J. Lipkova, S. Schlecht, F. Ahmaddy, S. Tatavarty, M. Bickel, P. Bilic, M. Rempfler, F. Hofmann, M. D. Anastasi, S.-A. Ahmadi, G. Kaissis, J. Holch, W. Sommer, R. Braren, V. Heinemann, B. Menze, Automatic Liver and Tumor Segmentation of CT and MRI Volumes Using Cascaded Fully Convolutional Neural Networks, 2017, pp. 1–20, arXiv:1702.05970v2.

[31] H.R. Roth, H. Oda, X. Zhou, N. Shimizu, Y. Yang, Y. Hayashi, M. Oda, M. Fujiwara, K. Misawa, K. Mori, An application of cascaded 3D fully convolutional networks for medical image segmentation, Comput. Med. Imag. Graph. 66 (2018) 90–99, https://doi.org/10.1016/j.compmedimag.2018.03.001.
[32] O. Ronneberger, P. Fischer, T. Brox, U-Net, Convolutional Networks for Biomedical Image Segmentation, 2015, pp. 1–8, arXiv:1505.04597. 9351.
[33] H. Noh, S. Hong, B. Han, Learning deconvolution network for semantic segmentation, in: Proc. IEEE Int. Conf. Comput. Vis. 2015 Inter, 2015, pp. 1520–1528, https://doi.org/10.1109/ICCV.2015.178.
[34] G. Litjens, T. Kooi, B.E. Bejnordi, A.A.A. Setio, F. Ciompi, M. Ghafoorian, J.A.W. M. van der Laak, B. van Ginneken, C.I. Sánchez, A survey on deep learning in medical image analysis, Med. Image Anal. 42 (2017) 60–88, https://doi.org/10.1016/j.media.2017.07.005.
[35] D. Shen, G. Wu, H.-I. Suk, Deep learning in medical image analysis, Annu. Rev. Biomed. Eng. 19 (2017) 221–248, https://doi.org/10.1146/annurev-bioeng-071516-044442.
[36] S. Ioffe, C. Szegedy, Batch Normalization : accelerating deep network training by reducing internal covariate shift, 2015, pp. 1–11, arXiv:1502.03167v3.
[37] C. Lee, P.W. Gallagher, Generalizing Pooling Functions in Convolutional Neural Networks: Mixed, Gated, and Tree, 2015, pp. 1–11, arXiv:1509.08985v2.
[38] A. Krizhevsky, G.E. Hinton, ImageNet classification with deep convolutional neural networks, NIPS'12 Proc. 25th Int. Conf. 1 (2012) 1–9.
[39] X. Glorot, A. Bordes, Deep sparse rectifier neural networks, Proc. Fourteenth Int. Conf. Artif. Intell. Stat. 15 (2011) 315–323.
[40] H. Zhao, O. Gallo, I. Frosio, J. Kautz, Loss Functions for Image Restoration with Neural Networks, 2018, pp. 1–11, arXiv:1511.08861v3.
[41] P. Isola, A.A. Efros, B. Ai, U.C. Berkeley, Image-to-Image Translation with Conditional Adversarial Networks, 2017, pp. 1–17, arXiv:1611.07004v2.
[42] A. Krogh, A simple weight decay can improve, NIPS'91 Proc. 4th Int. Conf. (1991) 950–957.
[43] M. Abadi, A. Agarwal, P. Barham, E. Brevdo, Z. Chen, C. Citro, G.S. Corrado, A. Davis, J. Dean, M. Devin, S. Ghemawat, I. Goodfellow, A. Harp, G. Irving, M. Isard, Y. Jia, R. Jozefowicz, L. Kaiser, M. Kudlur, J. Levenberg, D. Mane, R. Monga, S. Moore, D. Murray, C. Olah, M. Schuster, J. Shlens, B. Steiner, I. Sutskever, K. Talwar, P. Tucker, V. Vanhoucke, V. Vasudevan, F. Viegas, O. Vinyals, P. Warden, M. Wattenberg, M. Wicke, Y. Yu, X. Zheng, TensorFlow: Large-Scale Machine Learning on Heterogeneous Distributed Systems, 2016, pp. 1–19, arXiv:1603.04467.
[44] T. Rohlfing, Incorrect ICBM-DTI-81 atlas orientation and white matter labels, Front. Neurosci. 7 (2013) 2–5, https://doi.org/10.3389/fnins.2013.00004.
[45] H.A. David, J.L. Gunnink, The paired t test under artificial pairing the paired t test under artificial pairing, Am. Stat. 51 (1997) 9–12, https://doi.org/10.1080/00031305.1997.10473578.
[46] B.D.C. Van Essen, D. Ph, M.F. Glasser, D. Ph, The Human Connectome Project : Progress and Prospects, Cerebrum (2016) 1–16.
[47] T. Simuni, A. Siderowf, S. Lasch, C.S. Coffey, C. Caspell-garcia, D. Jennings, C. M. Tanner, J.Q. Trojanowski, L.M. Shaw, J. Seibyl, N. Schuff, A. Singleton, K. Kieburtz, A.W. Toga, B. Mollenhauer, D. Galasko, L.M. Chahine, D. Weintraub, Longitudinal change of clinical and biological measures in early Parkinson ' s Disease : Parkinson ' s progression markers initiative cohort, Mov. Disord. 33 (2018) 771–782, https://doi.org/10.1002/mds.27361.
[48] R.C. Petersen, P.S. Aisen, L.A. Beckett, M.C. Donohue, A.C. Gamst, D.J. Harvey, C. R. Jack, W.J. Jagust, L.M. Shaw, A.W. Toga, J.Q. Trojanowski, M.W. Weiner, Alzheimer's disease neuroimaging initiative (ADNI): clinical characterization, Neurology 74 (2009) 201–209, https://doi.org/10.1212/WNL.0b013e3181cb3e25.
[49] R.C. Petersen, G.E. Smith, S.C. Waring, R.J. Ivnik, E.G. Tangalos, E. Kokmen, Mild cognitive impairment: clinical characterization and outcome, Arch. Neurol. 56 (1999) 303–308, https://doi.org/10.1001/archneur.56.3.303.
[50] J. Yosinski, J. Clune, Y. Bengio, H. Lipson, How Transferable Are Features in Deep Neural Networks ?, 2014, pp. 1–14, arXiv:1411.1792.
[51] J.D. Van Horn, A.W. Toga, Multi-Site neuroimaging trials, Curr. Opin. Neurol. 22 (2009) 370–378, https://doi.org/10.1097/WCO.0b013e32832d92de.
[52] J. Jovicich, S. Czanner, D. Greve, E. Haley, A. Van Der Kouwe, R. Gollub, D. Kennedy, F. Schmitt, G. Brown, J. Macfall, B. Fischl, A. Dale, Reliability in multi-site structural MRI studies : effects of gradient non-linearity correction on phantom and human data, Neuroimage 30 (2006) 436–443, https://doi.org/10.1016/j.neuroimage.2005.09.046.
[53] T.M. Nir, N. Jahanshad, J.E. Villalon-reina, A.W. Toga, C.R. Jack, M.W. Weiner, P. M. Thompson, Effectiveness of regional DTI measures in distinguishing Alzheimer's disease, MCI, and normal aging, NeuroImage Clin. 3 (2013) 180–195, https://doi.org/10.1016/j.nicl.2013.07.006.
[54] A. Fellgiebel, I. Yakushev, Diffusion tensor imaging of the Hippocampus in MCI and early Alzheimer's disease, J. Alzheimer's Dis. 26 (2011) 257–262, https://doi.org/10.3233/JAD-2011-0001.
[55] C.D. Mayo, E.L. Mazerolle, L. Ritchie, J.D. Fisk, J.R. Gawryluk, Longitudinal changes in microstructural white matter metrics in Alzheimer s disease, NeuroImage Clin. 13 (2017) 330–338, https://doi.org/10.1016/j.nicl.2016.12.012.
[56] A. Larroza, D. Moratal, V.D. Alcañiz, E. Arana, Tractography of the uncinate fasciculus and the posterior cingulate fasciculus in patients with mild cognitive impairment and Alzheimer disease, Neurologia 29 (2014) 11–20, https://doi.org/10.1016/j.nrl.2013.02.002.
[57] K. Kichikawa, T. Kishimoto, Uncinate fasciculus-correlated cognition in Alzheimer's disease : a diffusion tensor imaging study by tractography, Psychogeriatrics 10 (2010) 15–20, https://doi.org/10.1111/j.1479-8301.2010.00312.x.
[58] A.M. Racine, N. Adluru, A.L. Alexander, B.T. Christian, O.C. Okonkwo, J. Oh, C. A. Cleary, A. Birdsill, A.T. Hillmer, D. Murali, T.E. Barnhart, C.L. Gallagher, C. M. Carlsson, H.A. Rowley, N.M. Dowling, S. Asthana, M.A. Sager, B.B. Bendlin, S. C. Johnson, Associations between white matter microstructure and amyloid burden in preclinical Alzheimer s disease : a multimodal imaging investigation, NeuroImage Clin. 4 (2014) 604–614, https://doi.org/10.1016/j.nicl.2014.02.001.
[59] A. Aitken, C. Ledig, L. Theis, J. Caballero, Z. Wang, W. Shi, Checkerboard Artifact Free Sub-pixel Convolution: A Note on Sub-pixel Convolution, Resize Convolution and Convolution Resize, 2017, pp. 1–16, arXiv:1707.02937.
[60] Augustus Odena, V. Dumoulin, C. Olah, Deconvolution and checkerboard artifacts, Distill 10 (2016) e3, https://doi.org/10.23915/distill.00003.
[61] A. Dosovitskiy, P. Fischer, E. Ilg, P. Häusser, C. Hazirbas, V. Golkov, P. van der Smagt, D. Cremers, T. Brox, Flownet: learning optical flow with convolutional networks, IEEE Int. Conf. Comput. Vis. (2015) 2758–2766, https://doi.org/10.1109/ICCV.2015.316, 2015.
[62] Hongyang Gao, Pixel Deconvolutional Networks, 2017, pp. 1–11, arXiv:1705.06820.
[63] S.M. Assari, H. Idrees, M. Shah, Perceptual losses for real-time style transfer and super-resolution, Proc. Eur. Conf. Comput. Vis. (2016) 694–711, https://doi.org/10.1007/978-3-319-46475-6.
[64] A. Radford, L. Metz, S. Chintala, Unsupervised Representation Learning with Deep Convolutional Generative Adversarial Networks, 2015, pp. 1–16, arXiv:1511.06434.
[65] WU - Minn Consortium, Human Connectome Project, Wu-Minn HCP 1200 Subjects Data Release: Reference Manual, 2017.